



Research paper

Computational micromechanics of porous brittle solids

Lars Blatny^a, Henning Löwe^b, Stephanie Wang^c, Johan Gaume^{a,b,*}^a School of Architecture, Civil and Environmental Engineering, Swiss Federal Institute of Technology, Lausanne, Switzerland^b WSL Institute for Snow and Avalanche Research SLF, Davos Dorf, Switzerland^c Department of Computer Science and Engineering, University of California, San Diego, La Jolla, USA

ARTICLE INFO

Keywords:

Porous brittle solids
 Finite strain elastoplasticity
 Material point method
 Microstructure-based modeling
 Gaussian random fields
 Failure

ABSTRACT

Porous brittle solids evidence complex mechanical behavior, where localized failure patterns originate from mechanical processes on the microstructural level. In order to investigate the failure mechanics of porous brittle solids, we outline a general stochastic and numerical microstructure-based approach. To this end, we generate random porous microstructures by level-cutting Gaussian random fields, and conduct numerical simulations using the material point method. This allows investigating both small and large deformation characteristics of irregular porous media where a segmentation into grains and bonds is ambiguous. We demonstrate the versatility of our approach by examining elasticity and failure as a function of a wide range of porosities, from 20% to 80%. Observing that onset of failure can be well described through the second order work, we show that the stress at failure follows a power law similar to that of the elastic modulus. Moreover, we propose that the failure envelope can be approximated by a simple quadratic fitting curve, and that plastic deformation appears to be governed by an associative plastic flow rule. Finally, large deformation simulations reveal a transition in the mode of localization of the deformation, from compaction bands for highly porous samples to shear bands for denser ones.

1. Introduction

Porous brittle materials which consist of a solid and void phase, such as rocks, snow, ceramics and foam, exhibit complex mechanical phenomena whose origin and overall characteristics are still not fully understood. This includes, e.g., the observation of so-called anticracks (Fletcher and Pollard, 1981) or compaction bands (Sternlof et al., 2005; Guillard et al., 2015), which in turn can be related to the more general question of how failure occurs, localizes and propagates in various media. In the geosciences, this question is crucial for the understanding of the preceding mechanisms of earthquakes (Green et al., 1990), landslides (Zhang et al., 2015) and avalanches (Heierli et al., 2008; Gaume et al., 2017a, 2018). The mechanical behavior of porous brittle materials, including elasticity, failure strength and plastic collapse, depends on the microstructure. Thus, in order to understand and realistically model the effective response of such materials, a microstructure-based approach is required, accounting for porosity and morphological variability.

Analytical microstructure-based investigations of effective properties of porous media are possible under certain assumptions and geometries. In general two-phase media, the well-known analytical results by Hashin and Shtrikman (1963) provide second-order bounds on the

effective elastic modulus, depending only on the phase moduli and volume fractions. For cellular solids, Gibson and Ashby (1982) derive the elastic modulus and collapse strength as being proportional to a power of the fraction of solid volume in the material, where the exponent depends on the type of cellular structure. Moreover, based only on the porosity and solid phase strength, Gurson (1977) analytically derived a yield surface for perfectly-plastic voided materials. This model was later extended by introducing empirical fitting parameters, now known as the Gurson–Tvergaard–Needleman (GTN) model (Tvergaard, 1981; Tvergaard and Needleman, 1984). The above-mentioned analytical studies are naturally limited by the simplifying assumptions, e.g., the geometrically regular premise of periodic unit cells, and not considering more complex microstructural models and variability. In the case of the Gibson and Ashby model, this leads to a mechanical behavior with too weak power law dependence Silva and Gibson (1997).

As a remedy, numerical simulations have aided researchers in determining the effective properties based on more complex geometrical and material properties of the microstructure. Through simulations with the finite element method (FEM), both Bruno et al. (2011) and Roberts and Garboczi (2000) showed how a power law relation between the elastic modulus and porosity changes depending on the microstructural pore shapes. With simulations based on the discrete element method

* Corresponding author at: School of Architecture, Civil and Environmental Engineering, Swiss Federal Institute of Technology, Lausanne, Switzerland.
 E-mail address: johan.gaume@epfl.ch (J. Gaume).

(DEM), Gaume et al. (2017b) studied the mechanical behavior of porous microstructures represented as sticky hard spheres, relating the elastic modulus and compressive strength to the contact density instead of porosity. Using the same simulation setup, Ritter et al. (2020) extended this study of highly porous microstructures by deriving an elliptic failure envelope and evidenced an associated plastic flow law. As an alternative to idealized microstructures, geometries obtained from X-ray micro-computed tomography of real materials as input to FEM (Petit et al., 2013) or DEM (Hagenmuller et al., 2015) simulations have shown to be promising in investigating the mechanics of porous brittle media. Moreover, double scale approaches that couple the microscale resolved by DEM at each integration point in FEM on the macroscale have been proposed (Desrues et al., 2014; Guo and Zhao, 2014; Zhao et al., 2020).

Although numerical upscaling of elasticity and yielding of arbitrary microstructures of porous geomaterials is standard (using FEM), numerical methods to study generic features of the transition from small to large strain situations that involve yielding and failure are missing. Treating this transition is feasible for spherical/particulate microstructures using DEM. However, many materials cannot be described by such geometries, while flexible computational approaches for arbitrary bicontinuous microstructures are still missing. This prevents the development of accurate homogenized constitutive models for these materials. It is therefore the aim of the present paper to use the material point method (MPM) on randomly structured, bicontinuous microstructures to show the suitability of this combination for exploring generic effects of elasticity, yield, softening and failure localization in porous brittle solids with non-spherical/non-particulate microstructures. We focus here on the changes in these quantities with solid volume fraction as the most important control on the mechanical behavior.

We first give a short presentation of the computational generation of bicontinuous microstructures, which will be generated by level-cutting Gaussian random fields. Through this procedure, we can obtain ensembles of random geometries with given solid volume fraction and other properties. Our work can thus be regarded a generalization of the work by Roberts and Garboczi (2002) who were studying the small strain behavior of these systems using FEM. Next, we formulate an elastoplastic model used to describe the solid matrix of the microstructures in the context of finite strain elastoplasticity theory. Employing triaxial loading MPM simulations and defining effective failure through a second order work criterion, we evaluate our approach by presenting and discussing elasticity/failure power laws, failure envelopes, and failure mechanics in large deformation simulations.

2. Methods

2.1. Stochastic microstructures

A computationally efficient method for generating two-phase microstructures is through level-cutting Gaussian random fields (GRF), the mathematical formalism of which was first outlined by Cahn (1965). This approach allows realizing stochastic structures with certain prescribed properties, most importantly the solid volume fraction. The procedure can be summarized as follows. Consider a GRF, $G(\mathbf{r})$, as a superposition of $N_c \gg 1$ sinusoidal waves,

$$G(\mathbf{r}) = \frac{1}{\sqrt{N_c}} \sum_{n=1}^{N_c} \cos(\boldsymbol{\eta}_n \cdot \mathbf{r} + \varphi_n) \quad (1)$$

where the φ_n are independent, identically distributed random variables in $[0, 2\pi]$ and $\boldsymbol{\eta}_n$ is the wave vector. As suggested by Ding et al. (2010), the wave vector's magnitude $\eta \equiv 2\pi/\omega$ can be sampled from the gamma distribution function

$$P(\eta) = \frac{(b+1)\Gamma(b+1)}{\langle \eta \rangle \Gamma(b+1)} \left(\frac{\eta}{\langle \eta \rangle} \right)^b e^{-(b+1)\frac{\eta}{\langle \eta \rangle}} \quad (2)$$

where $b > 0$ is a parameter adjusting the width of the distribution and thus controls the variation in the spatial extent of the solid phase, i.e., the heterogeneity of the structure. A large value $b \gg 1$ gives a narrow distribution, resulting in a structure with small degree of structural heterogeneity, i.e., an approximately homogeneous structure. Moreover, $\langle \eta \rangle$ is the prescribed mean wave vector magnitude and sets a mean number of "solid phase units". In order to obtain isotropic microstructures, which will be the case throughout this paper, we sample the directions of the wave vector from the unit sphere. However, if anisotropic microstructures are desired, the sampling can simply be restricted to a subset of the unit sphere as shown by Tan et al. (2016). A microstructure $M(\mathbf{r})$ of the form

$$M(\mathbf{r}) = \begin{cases} 1, & \text{if } \mathbf{r} \in \text{solid phase} \\ 0, & \text{if } \mathbf{r} \notin \text{solid phase.} \end{cases} \quad (3)$$

is obtained by level-cutting $G(\mathbf{r})$ to the desired ice volume fraction ϕ such that

$$M(\mathbf{r}) = \begin{cases} 1, & \text{if } G(\mathbf{r}) > \text{erf}^{-1}(1 - 2\phi) \\ 0, & \text{otherwise} \end{cases} \quad (4)$$

where $\text{erf}^{-1}(\cdot)$ denotes the inverse error function. The reader is referred to Appendix B for more details about the characteristics of the microstructures used in this work.

2.2. Elastoplastic model

Numerically modeling the effective mechanical behavior of porous materials requires a constitutive model for the solid phase. In this section, we formulate such model in the framework of finite strain elastoplasticity theory. Defining the deformed and undeformed coordinate \mathbf{x} and \mathbf{X} , respectively, we make use of the common assumption of decomposing the second-order tensor known as the deformation gradient $\mathbf{F} = \partial\mathbf{x}/\partial\mathbf{X}$ into an elastic and a plastic part as $\mathbf{F} = \mathbf{F}^E \mathbf{F}^P$. In this setting, we model the solid phase with a frame-indifferent, isotropic, hyperelastic model described by a strain energy density function $\Psi(\mathbf{F}^E)$ and a yield criterion defining the onset of plastic, irreversible, deformations. Specifically, we use the St. Venant-Kirchhoff elastic model, expressed with the elastic Hencky strain tensor

$$\boldsymbol{\varepsilon}^E = \frac{1}{2} \sum_{i=1}^3 \log \lambda_i^2 \mathbf{n}_i \otimes \mathbf{n}_i \quad (5)$$

where λ_i are the principal stretches whose square are the eigenvalues of the left Cauchy–Green deformation tensor $\mathbf{b}^E = \mathbf{F}^E (\mathbf{F}^E)^T$ with corresponding eigenvectors \mathbf{n}_i . The St. Venant-Kirchhoff strain energy density function can then be expressed as

$$\Psi(\mathbf{F}^E) = \frac{1}{2} \lambda (\text{tr } \boldsymbol{\varepsilon}^E)^2 + \mu \text{tr}(\boldsymbol{\varepsilon}^E : \boldsymbol{\varepsilon}^E) \quad (6)$$

where $\lambda = \frac{E\nu}{(1+\nu)(1-2\nu)}$ and $\mu = \frac{E}{2(1+\nu)}$ are the Lamé parameters which can be related to the Young's modulus E and Poisson's ratio ν . Introducing the second order Kirchhoff stress tensor $\boldsymbol{\tau} = \frac{\partial\Psi(\mathbf{F}^E)}{\partial\mathbf{F}^E} (\mathbf{F}^E)^T$ gives the following stress–strain relationship,

$$\boldsymbol{\tau} = \mathbf{C} : \boldsymbol{\varepsilon}^E = \lambda (\text{tr } \boldsymbol{\varepsilon}^E) \mathbf{I} + 2\mu \boldsymbol{\varepsilon}^E. \quad (7)$$

Note that the Kirchhoff stress $\boldsymbol{\tau}$ is related to the Cauchy stress $\boldsymbol{\sigma}$ through $\boldsymbol{\tau} = \det(\mathbf{F})\boldsymbol{\sigma}$. The choice of using a model based on Hencky strain, as opposed to e.g. the Green strain, makes the elastoplastic numerical integration scheme more convenient (Mast, 2013). The elastic model presented here has been successfully used in various publications on material point method modeling (Mast, 2013; Klár et al., 2016; Gaume et al., 2018).

Geomechanical, polymeric and various other porous materials usually consist of a solid phase that is pressure-dependent, and thus a simple von Mises yield criterion is insufficient for accurately capturing the onset of plastic deformation. For this reason, the Drucker–Prager

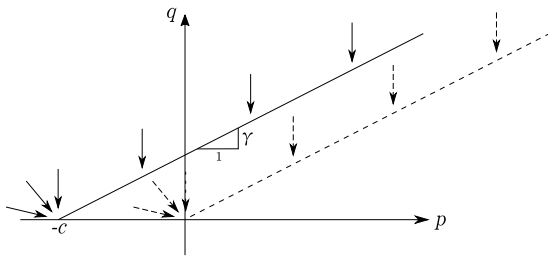


Fig. 1. The yield surface $y(p, q) = 0$ of the Drucker–Prager strain softening model from Eq. (8). The dashed line represents the final yield surface as $\epsilon_s^p \rightarrow \infty$. The arrows represent the direction of the plastic flow.

model is often used as it introduces a linear pressure dependency to the von Mises model, also reflecting the observed asymmetry in tensile and compressive strengths. Furthermore, porous brittle solids exhibit strong softening after failure. Consequently, in order to account for the main physical processes outlined above in the simplest possible manner, we propose a strain softening Drucker–Prager model to describe the yielding of the solid phase of the GRF microstructures. This yield function will be expressed in the space of the two stress invariants $p = -\frac{1}{3} \text{tr } \boldsymbol{\tau}$ called the mean stress and $q = \sqrt{\frac{3}{2} \text{dev } \boldsymbol{\tau} : \text{dev } \boldsymbol{\tau}}$ called the von Mises equivalent stress, where we have defined the operator $\text{dev}(\cdot) = (\cdot) - \frac{1}{3} \text{tr}(\cdot) \mathbf{I}$. With these definitions, the proposed yield function is formulated as

$$y(p, q) = q - \gamma \left(p + ce^{-\xi \epsilon_s^p} \right) \quad (8)$$

with a non-associative flow rule as shown in Fig. 1. Here, the constant γ can be related to the material's friction angle, and $c > 0$ represents an initial cohesion. The constant $\xi > 0$ controls the degree of post-yield softening based on the accumulated amount of deviatoric plastic strain $\epsilon_s^p \equiv \sqrt{\text{dev}(\boldsymbol{\epsilon}^P) : \text{dev}(\boldsymbol{\epsilon}^P)}$, allowing us to adjust the brittleness of the material.

Yielding of the microstructure solid phase does not necessarily imply effective failure of the macroscopic porous material. Relying on Hill (1958), Nicot et al. (2009), Nicot and Darve (2015), Nicot et al. (2017) argue that such macroscopic failure can be defined more generally through the change of sign of the second order work

$$W_2 = \int_{\partial V} \dot{\mathbf{u}}(t) \cdot \dot{\mathbf{f}}(t) dS \quad (9)$$

where $\mathbf{u} = \mathbf{X} - \mathbf{x}$ is the displacement and \mathbf{f} is the resulting force on the boundary ∂V .

2.3. Numerical scheme

The mechanical response of microstructures subjected to loading is numerically modeled with the material point method (MPM) as a numerical scheme to approximate solutions to the mass and momentum conservation equations,

$$\frac{D\rho}{Dt} + \rho \nabla \cdot \mathbf{v} = 0, \quad \rho \frac{D\mathbf{v}}{Dt} = \nabla \cdot \boldsymbol{\sigma}, \quad (10)$$

where $\rho = \rho(\mathbf{x}, t)$ is the mass density, subject to an elastoplastic constitutive law as outlined in the previous section, and relevant initial and boundary conditions. Dating back to Sulsky et al. (1994), MPM is a hybrid Eulerian–Lagrangian numerical scheme for solving the continuum equations. In particular, it has gained attention for being especially suitable and convenient for large deformation solid mechanics modeling in the engineering and computer graphics community. This stems from discretizing space into particles, which track position, velocity, mass and deformation, combined with a background mesh which facilitates painless computation of spatial derivatives.

In the present study, we consider solid structures discretized into a finite number N_p of particles with constant and equal mass m_p , initially

equal volume V_p and initially zero velocity \mathbf{v}_p . Given a background grid with uniform grid spacing Δx , we consider interpolation functions between a grid node i and a particle p on the form

$$N_i(\mathbf{x}_p) = N \left(\frac{x_p - x_i}{\Delta x} \right) N \left(\frac{y_p - y_i}{\Delta x} \right) N \left(\frac{z_p - z_i}{\Delta x} \right) \quad (11)$$

where $N(u)$ is here taken to be the quadratic B-spline

$$N(u) = \begin{cases} \frac{3}{4} - |u|^2, & \text{if } |u| < \frac{1}{2} \\ \frac{1}{2} \left(\frac{3}{2} - |u| \right)^2, & \text{if } \frac{1}{2} \leq |u| < \frac{3}{2} \\ 0, & \text{otherwise.} \end{cases} \quad (12)$$

The background grid, which is considered regular and structured, has no hard boundary in the sense that a grid node is only activated by particles in its vicinity at each time step. Although there exist several variations of MPM, we have resorted to explicit time integration and a weighted combination of the particle-in-cell (PIC) and fluid-implicit-particle (FLIP) method for grid-particle interpolation, as presented and used by, e.g., Klár et al. (2016), Gaume et al. (2018). In Algorithm 1 we outline in details the steps of the MPM used in this work, and in Algorithm 2 more details are provided on the computation of the return mapping procedure involved with the strain softening Drucker–Prager criterion outlined in the previous section.

Algorithm 1: Elastoplastic explicit Euler B-spline PIC-FLIP MPM

initialize $m_p, V_p, \mathbf{x}_p, \mathbf{v}_p = \mathbf{0}, \mathbf{F}^E = \mathbf{I}, \epsilon_s^p = 0$

for $n \leftarrow 0$ **to** *max time steps* **do**

1. adapt time step: $\Delta t = \min \left(C_{\text{CFL}} \frac{\Delta x}{\max_p |\mathbf{v}_p^n|}, C_{\text{el}} \frac{\Delta x}{\sqrt{E/\rho}} \right)$
2. interpolate grid mass: $m_i^n = \sum_{p=1}^{N_p} m_p N_i(\mathbf{x}_p^n)$
3. interpolate grid velocity: $\mathbf{v}_i^n = \frac{1}{m_i^n} \sum_{p=1}^{N_p} m_p \mathbf{v}_p^n N_i(\mathbf{x}_p^n)$
4. get grid force: $\mathbf{f}_i^n = - \sum_{p=1}^{N_p} V_p^0 \frac{\partial \Psi(\mathbf{F}_p^{E,n})}{\partial \mathbf{F}^E} (\mathbf{F}_p^{E,n})^T \nabla N_i(\mathbf{x}_p^n)$
5. update grid velocity: $\mathbf{v}_i^{n+1} = \mathbf{v}_i^n + \frac{\Delta t}{m_i^n} \mathbf{f}_i^n$
6. apply boundary conditions to the grid velocities
7. get trial elastic deformation gradient on the particles: $\mathbf{F}_p^{E,\text{trial}} = \left(\mathbf{I} + \Delta t \sum_{i \in \text{grid}} \mathbf{v}_i^{n+1} (\nabla N_i(\mathbf{x}_p^n))^T \right) \mathbf{F}_p^{E,n}$
8. perform SVD of $\mathbf{F}_p^{E,\text{trial}} = \mathbf{U}_p^E \boldsymbol{\Sigma}_p^{E,\text{trial}} (\mathbf{V}_p^E)^T$
9. get trial elastic Hencky strain: $\boldsymbol{\epsilon}_p^{E,\text{trial}} = \ln \boldsymbol{\Sigma}_p^{E,\text{trial}}$
10. return mapping: Get $\boldsymbol{\epsilon}_p^{E,n+1}$ from $\boldsymbol{\epsilon}_p^{E,\text{trial}}$ using Algorithm 2
11. update elastic deformation gradient on the particles $\mathbf{F}_p^{E,n+1} = \mathbf{U}_p^E e^{\boldsymbol{\epsilon}_p^{E,n+1}} (\mathbf{V}_p^E)^T$
12. update particle velocity: $\mathbf{v}_p^{n+1} = \alpha_f \mathbf{v}_p^{\text{FLIP}} + (1 - \alpha_f) \mathbf{v}_p^{\text{PIC}}$ where $\mathbf{v}_p^{\text{PIC}} = \sum_{i \in \text{grid}} \mathbf{v}_i^{n+1} N_i(\mathbf{x}_p^n)$, $\mathbf{v}_p^{\text{FLIP}} = \mathbf{v}_p^n + \sum_{i \in \text{grid}} (\mathbf{v}_i^{n+1} - \mathbf{v}_i^n) N_i(\mathbf{x}_p^n)$
13. update positions: $\mathbf{x}_i^{n+1} = \mathbf{x}_i^n + \Delta t \mathbf{v}_i^{n+1}$, $\mathbf{x}_p^{n+1} = \sum_{i \in \text{grid}} \mathbf{x}_i^{n+1} N_i(\mathbf{x}_p^n)$

end

comment: $C_{\text{CFL}}, C_{\text{el}}$ and $\alpha_f \in [0, 1]$ are appropriate constants chosen to obtain a stable scheme. We have found $C_{\text{CFL}} = 0.6$, $C_{\text{el}} = 0.5$ and $\alpha_f = 0.99$ to give stable results for our simulations.

2.4. Simulation setup

We let GRF microstructures be subjected to displacement-controlled triaxial loading. Statistical fluctuations of the structures are accounted for by simulating and averaging over several realizations for given GRF parameters, in particular the solid volume fraction ϕ . In this work,

Algorithm 2: Return mapping for the strain softening non-associative Drucker–Prager model introduced in Eq. (8) and Fig. 1

```

input   :  $\epsilon_p^{E,\text{trial}}, \epsilon_{S,p}^P$ 
output  :  $\epsilon_p^{E,n+1}, \epsilon_{S,p}^P$ 
define  :  $K = \lambda + 2\mu/3$ 
 $\delta\pi_p = |\text{dev}(\epsilon_p^{E,\text{trial}})| + \frac{\gamma}{\sqrt{6}\mu} \left( K \text{tr}(\epsilon_p^{E,\text{trial}}) - ce^{-\xi\epsilon_{S,p}^P} \right)$ 
if  $K \text{tr}(\epsilon_p^{E,\text{trial}}) \geq ce^{-\xi\epsilon_{S,p}^P}$  then
   $\epsilon_{S,p}^P += |\text{dev}(\epsilon_p^{E,\text{trial}})|$ 
   $\epsilon_p^{E,n+1} = \frac{c}{3K} e^{-\xi\epsilon_{S,p}^P} \mathbf{I}$ 
else if  $\delta\pi_p > 0$  then
   $\epsilon_{S,p}^P += \delta\pi_p$ 
   $\delta\pi_p^* = |\text{dev}(\epsilon_p^{E,\text{trial}})|$ 
  if  $K \text{tr}(\epsilon_p^{E,\text{trial}}) < ce^{-\xi\epsilon_{S,p}^P}$  then
     $\delta\pi_p^* += \frac{\gamma}{\sqrt{6}\mu} \left( K \text{tr}(\epsilon_p^{E,\text{trial}}) - ce^{-\xi\epsilon_{S,p}^P} \right)$ 
     $\epsilon_p^{E,n+1} = \delta\pi_p^* \frac{\text{dev}(\epsilon_p^{E,\text{trial}})}{|\text{dev}(\epsilon_p^{E,\text{trial}})|}$ 
  else
     $\epsilon_p^{E,n+1} = \frac{c}{3K} e^{-\xi\epsilon_{S,p}^P} \mathbf{I}$ 
  end
   $\epsilon_{S,p}^P += (\delta\pi_p^* - \delta\pi_p)$ 
else
   $\epsilon_p^{E,n+1} = \epsilon_p^{E,\text{trial}}$ 
end

```

comment: If the trial step returns a stress state with mean stress smaller than permitted by the yield criterion, the first if-statement is evaluated as true. The state is then projected to the “tip” of the yield surface as illustrated by the arrows to the left in Fig. 1. If instead the mean stress is to the right of the “tip”, but still outside the yield surface, the else if statement is evaluated as true. On the other hand, if the trial state is inside the yield surface, the final else statement is evaluated as true, and the trial state is accepted without modifications.

we apply our method only to isotropic samples with a low degree of structural heterogeneity. The microstructural and material parameters are summarized in Table 1 and taken to be representative of snow as a porous medium consisting of an ice skeleton.

While the Young’s modulus E_s and Poisson’s ratio ν_s of the solid phase (ice) are taken to be in the realistic range (Petrovic, 2003), the density ρ_s is chosen ten times larger than that of actual ice in order to speed up the simulations. In the absence of gravity, this modification results only in a time–velocity scaling, and it has been verified that the overall stress–strain behavior is unaffected by this choice. Moreover, the choice $\gamma = 1.2$ corresponds to a friction angle of 30 degrees for the solid phase (Aexeev et al., 2003). In addition, we assume for simplicity that the cohesion of a material point vanishes immediately after yielding, hence the choice of a large ξ . The size of the microstructures are chosen on the basis of a representative volume element convergence analysis in order to mitigate finite size effects, see Appendix A. The results of this analysis suggest a size of at least nine mean wavelengths $\langle\omega\rangle = 2\pi/\langle\eta\rangle$ per (shortest) side length L . For the purpose of the numerical simulations, the structures are discretized such that the microstructural shape and contour are sufficiently resolved on a $131 \times 131 \times 131$ regular particle grid. The background Eulerian grid is subsequently chosen to yield eight particles per grid cell.

The structures are subjected to deformation by displacing six surrounding “sticky” walls, each having a fixed velocity. Similar to Fritzen et al. (2012), we assume that two opposite walls have equal, but

Table 1
Microstructure and material parameters.

Parameter	Symbol	Value	Unit
Number of GRF waves	N_c	10^4	–
Relative mean GRF wavelength	$\langle\omega\rangle/L$	$1/9$	–
Degree of GRF heterogeneity	b	50	–
Solid phase density	ρ_s	10^4	kg/m ³
Solid phase Young’s modulus	E_s	10	GPa
Solid phase Poisson’s ratio	ν_s	0.3	–
Internal friction constant	γ	1.2	–
Internal cohesion	c	2.5	MPa
Degree of softening	ξ	10^6	–
Imposed strain rate	$\dot{\epsilon}^{\text{wall}}$	$5 \cdot 10^{-4}$	s ⁻¹

oppositely directed velocities such that the movement of the six walls can be described by the three strain rates

$$\begin{aligned} \dot{\epsilon}_x^{\text{wall}} &= (\beta_2 + \beta_1)\dot{\epsilon}^{\text{wall}} \\ \dot{\epsilon}_y^{\text{wall}} &= (\beta_2 - \beta_1)\dot{\epsilon}^{\text{wall}} \\ \dot{\epsilon}_z^{\text{wall}} &= \beta_2\dot{\epsilon}^{\text{wall}} \end{aligned} \quad (13)$$

through two variable parameters β_1 and β_2 . Here, $\dot{\epsilon}^{\text{wall}}$ is an imposed strain rate constant presented in Table 1. The two adjustable parameters β_1 and β_2 allow us to continuously transition between simulations of isotropic tension ($\beta_1 = 0, \beta_2 = 1$), through pure shear ($\beta_1 = 1, \beta_2 = 0$), to isotropic compression ($\beta_1 = 0, \beta_2 = -1$). The effective response of the system is evaluated by recording the volume-averaged mean stress $\langle p \rangle$ and von Mises equivalent stress $\langle q \rangle$. In the pure elastic regime, the effective bulk modulus K can be obtained by fitting to $\langle p \rangle = -K\epsilon_V$, where $\epsilon_V = 6t\beta_2\dot{\epsilon}^{\text{wall}}$ is the imposed macroscopic volumetric engineering strain. In addition, the effective failure of the overall structure is defined by the second order work criterion $W_2 = 0$. We denote the volume-averaged mean and von Mises equivalent stress at failure by $\langle p \rangle_f$ and von Mises equivalent stress $\langle q \rangle_f$, respectively.

3. Results

3.1. Elasticity and failure onset

Fig. 2 shows the volume-averaged mean stress $\langle p \rangle$ and von Mises equivalent stress $\langle q \rangle$ as a function of imposed strain for simulations in isotropic compression and pure shear, respectively. The corresponding evolution of the second order work is shown in Fig. 3 together with the failure criterion $W_2 = 0$. The computational cost of these simulations depends on the solid volume fraction as the mesh resolution and the parameters restricting the time step size (see Algorithm 1) remain constant. For a typical case of one million particles, the simulation time is roughly 75 min, or 0.09 s per time step. The computations were parallelized with Intel TBB on 48 Intel Xeon Gold 6136 processors.

Before yielding, i.e., $\gamma(p, q) < 0$, the mechanical response is purely elastic. The elastic response is stiffer with increasing solid volume fraction of the system. Correspondingly, the failure strength increases with solid volume fraction. In Fig. 4 we present the effective elastic bulk modulus K , shear modulus G and failure strengths $\langle p \rangle_f, \langle q \rangle_f$ as a function of solid volume fraction ϕ . We find that a simple power law in the solid volume fraction is applicable to describe our observations of both the elastic moduli and the failure strengths, in particular,

$$K \sim \phi^{3.22 \pm 0.03} \quad (14a)$$

$$G \sim \phi^{3.05 \pm 0.04} \quad (14b)$$

$$\langle p \rangle_f^c \sim \phi^{3.86 \pm 0.03} \quad (14c)$$

$$\langle p \rangle_f^t \sim \phi^{3.27 \pm 0.05} \quad (14d)$$

$$\langle q \rangle_f^s \sim \phi^{3.75 \pm 0.03} \quad (14e)$$

where the superscripts c, t and s refer to loading in isotropic compression, tension and pure shear, respectively. The provided uncertainty of the power law exponent is the standard error under the assumption of residual normality.

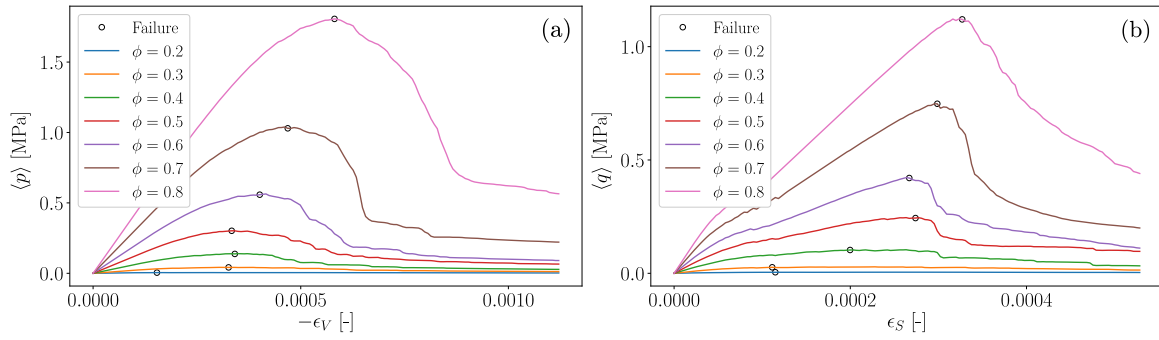


Fig. 2. Stress–strain curves for samples of various solid volume fractions ϕ under (a) isotropic compression loading and (b) pure shear loading. The failure point is marked for each simulation. Here, ϵ_V and ϵ_S represent volumetric and shear engineering strain, respectively.

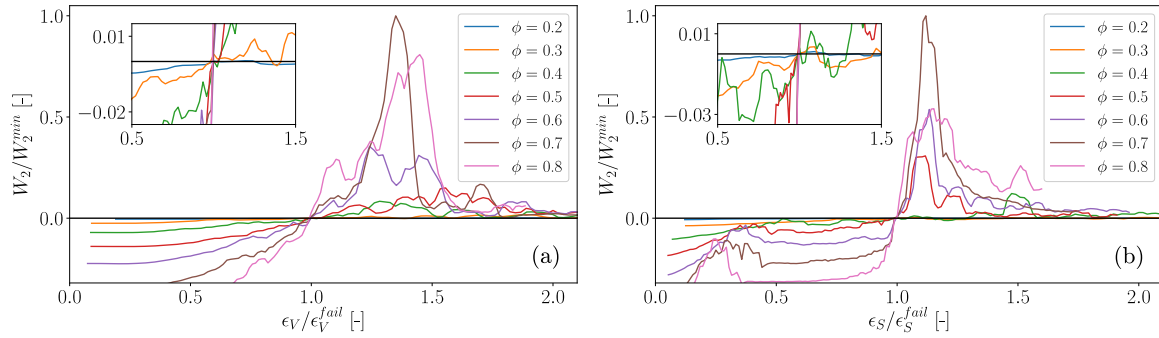


Fig. 3. Normalized second order work for samples of various solid volume fractions ϕ under (a) isotropic compression loading and (b) pure shear loading. It is normalized through a scaling by the observed minimum second order work of all samples. Since samples will fail at different imposed deformations, the strain axis is here normalized according to the strain at failure. The $W_2 = 0$ failure criterion is marked by a solid black line, and the inset plots provides a zoom view of the failure line crossing.

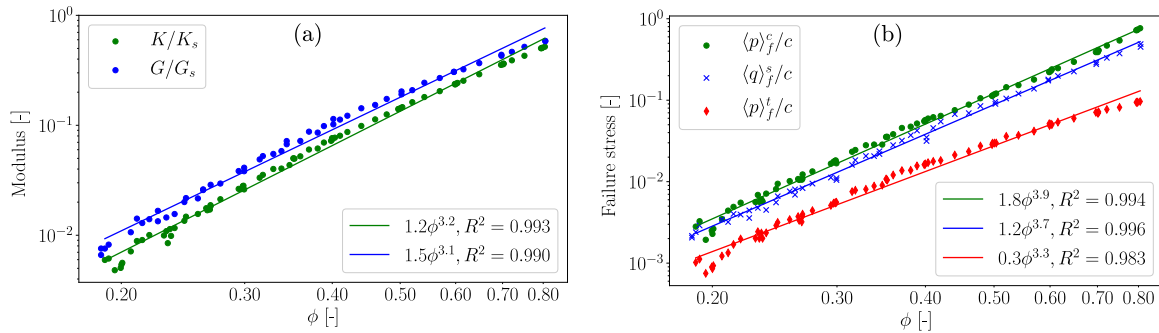


Fig. 4. Evolution of (a) bulk and shear modulus and (b) stress at failure in isotropic compression, isotropic tension and pure shear, as a function of the solid volume fraction ϕ , presented in a log–log scale.

3.2. Failure envelope

Failure envelopes are presented in Fig. 5 in the space of volume-averaged mean and von Mises equivalent stress. Remarkably, we observe that over the full range of porosities studied, failure envelopes can be approximated reasonably well by a simple quadratic curve,

$$q(p) = \frac{2M}{2\beta + 1} \frac{(p_c - p)(\beta p_c + p)}{p_c} \quad (15)$$

where p_c represents the compressive strength, β gives the ratio of tensile to compressive strength and M is the cohesionless critical state line, in analogy to the cohesive Cam-clay model as used by Gaume et al. (2018).

In Fig. 5, we include our failure envelope model fitted according to the simulation data using ordinary least squares. This fitting yields coefficients of determination between $R^2 = 0.90$ (for $\phi = 0.2$) and $R^2 = 0.96$ (for $\phi = 0.266$). Interestingly, we find a mean value for M as 1.35 ± 0.14 and that β depends linearly on the solid volume fraction

through $\beta = 0.43 - 0.40\phi$ with $R^2 = 0.991$. Collapsing the data onto the unit quadratic parabola, we display in Fig. 6 the failure points in the space of the correspondingly transformed variables $\langle p \rangle^* = \frac{2p/p_c + \beta - 1}{\beta + 1}$ and $\langle q \rangle^* = \frac{2}{M} \frac{2\beta + 1}{(\beta + 1)^2} \frac{q}{p_c}$.

Studying the stress paths followed after failure, it appears that an associative flow rule is an appropriate choice for smaller solid volume fractions, see Fig. 7a. In this case, the stress follows roughly the gradient to the failure envelope. For larger solid volume fractions, as illustrated in Fig. 7b, the situation becomes more complex due to the enhanced difference between tensile and compressive failure. However, the direction of the stress paths after failure is still well approximated by the envelope normal.

3.3. Large strain failure behavior

So far, we have investigated the elastic and failure regimes which take place at relatively small deformations. In order to further evaluate our general numerical approach, we perform large deformation

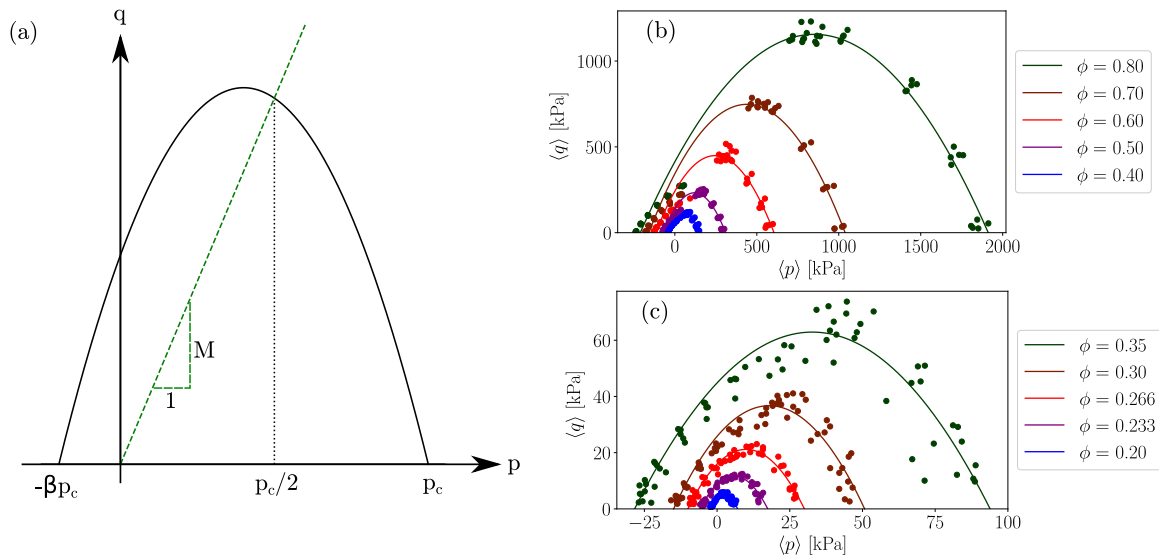


Fig. 5. Failure envelopes. The model of Eq. (15) is illustrated in (a) and its fit to the data is shown in (b) and (c). The observed failure points from the simulations are marked as dots. For each structure, 13 different combinations of (β_1, β_2) are chosen to explore the stress space.

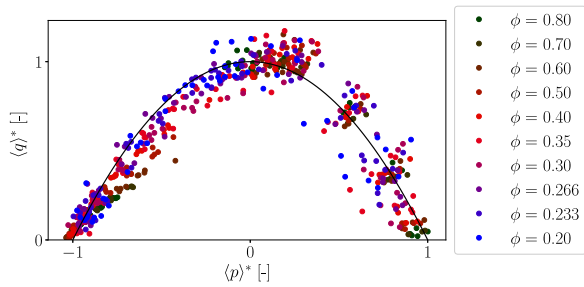


Fig. 6. Failure envelopes for all structures normalized to the unit quadratic parabola.

simulations on microstructures in uniaxial confined compression with zero-friction slipping boundary conditions. Specifically, we study microstructures with various initial solid volume fractions ($\phi = 0.24, 0.34, 0.44, 0.54$ and 0.70) and aspect ratio 2:1, elongated in the direction of compression, in order to better study the spatial propagation of failure. Fig. 8 visualizes the velocity distribution in the samples studied. Areas displaying higher velocity gradients are accompanied by higher plastic strain rates, visualized in Fig. 9. Fig. 10 shows the accumulated plastic strain.

Different failure features can be observed depending on the initial solid volume fraction. Failure is initiated at the top near the compressive plate for samples with low solid volume fraction, while closer to

the middle of the sample when the solid volume fraction is higher. The reader is referred to the supplementary videos for the temporal evolution of these samples. In simulations of the samples with the two lowest initial solid volume fractions, a compaction band (a narrow horizontal zone of localized deformation) propagates from the top of the sample in the vertical direction of compression. In the samples with higher solid volume fractions, shear bands are initiated closer to the middle of the structure.

Fig. 11a shows how the volume-averaged mean stress changes with imposed deformation until the structures are fully compacted, i.e., reached a jamming state. Correspondingly, Fig. 11b displays the evolution of the inverse solid volume fraction in these large deformation simulations as a function of the macroscopic mean stress. We can divide the deformation into different stages: the initial elastic and yielding stage until failure, post-failure softening, plastic consolidation or collapse, and finally densification/jamming. Using this classification, we display the stress evolution in Fig. 12 in the case of the initial solid volume fraction being 0.34. In the densification stage of this structure, we observe an effective friction angle of 20 degrees ($q \approx 0.75p$).

4. Discussion

The results of our numerical experiments, presented in the previous section, highlight universal relationships of elasticity and failure with solid volume fraction in porous brittle solids. In order to substantiate the general and stochastic microstructure-based approach proposed in

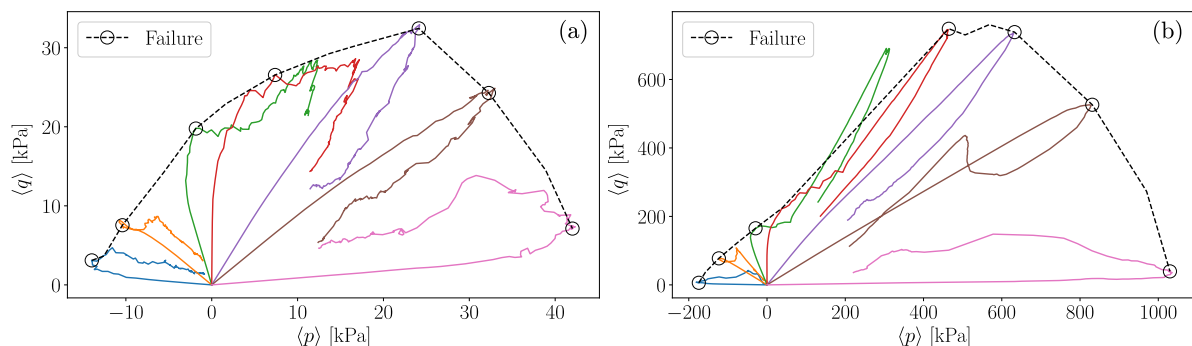


Fig. 7. Selected stress paths followed in two structures of different solid volume fraction ϕ , (a) $\phi = 0.30$, (b) $\phi = 0.70$. The failure points and envelopes are marked. The different stress paths, marked by colored lines, are obtained by altering the loading through (β_1, β_2) in Eq. (13).

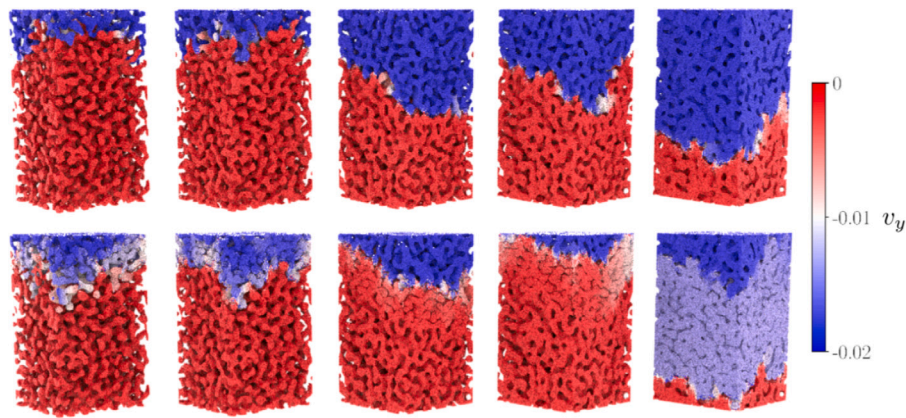


Fig. 8. Vertical component of velocity v_y visualized in microstructures with various initial solid volume fractions $\phi = 0.24, 0.34, 0.44, 0.54, 0.70$, from left to right. The top row is taken at $\epsilon_v = -0.4\%$, the bottom at $\epsilon_v = -11\%$. See also supplementary movie.

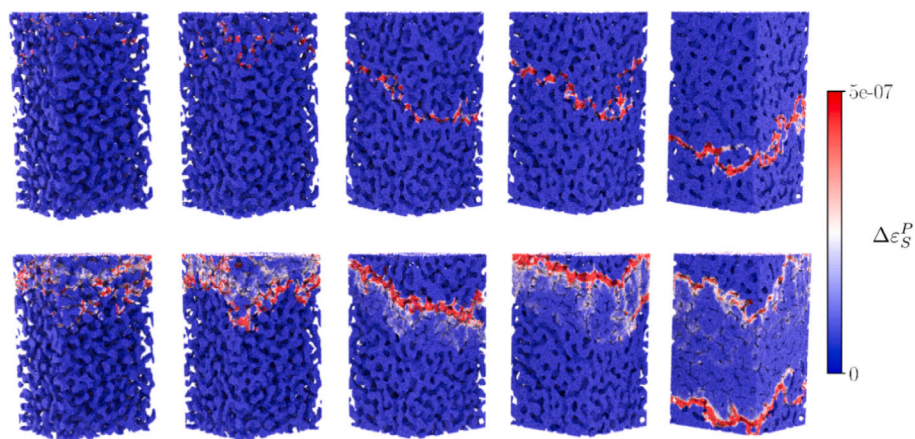


Fig. 9. Deviatoric plastic strain per time step $\Delta\epsilon_S^P$ visualized in microstructures with various initial solid volume fractions $\phi = 0.24, 0.34, 0.44, 0.54, 0.70$, from left to right. The top row is taken at $\epsilon_v = -0.4\%$, the bottom at $\epsilon_v = -11\%$. See also supplementary movie.

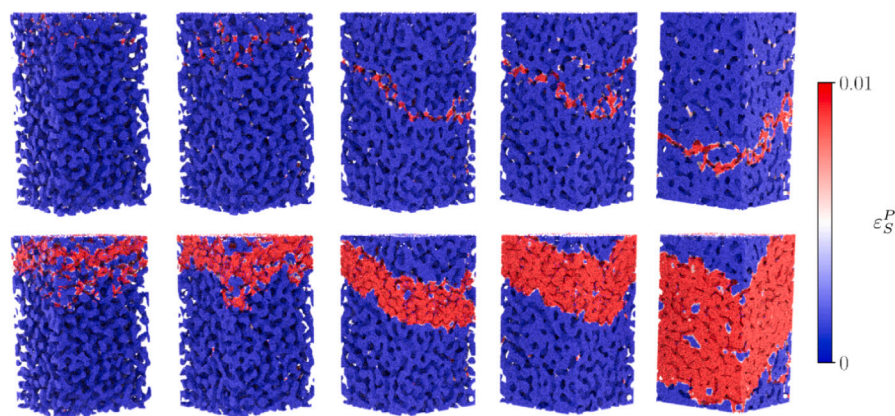


Fig. 10. Accumulated deviatoric plastic strain ϵ_S^P visualized in microstructures with various initial solid volume fractions $\phi = 0.24, 0.34, 0.44, 0.54, 0.70$, from left to right. The top row is taken at $\epsilon_v = -0.4\%$, the bottom at $\epsilon_v = -11\%$. See also supplementary movie.

this paper, we discuss in the following how these results relate to previous numerical and experimental observations.

Regarding elasticity and onset of failure, we see in Fig. 4 that a simple power law in the solid volume fraction ϕ can explain the evolution of bulk modulus and failure remarkably well. In the literature, several power laws for the elastic modulus and failure strength have been suggested. In particular, a Young’s modulus $E \sim \phi^m$ with $m \in [3, 5]$ is typically reported. It is argued that the exponent m reflects

the nature of the effective structural “backbone” of the system through which the stress is transmitted. This backbone is the part of the (percolating cluster of the) structure that carries the majority of the load and thus contributes the most to the overall deformation (Mewis and Wagner, 2011; Roy and Tirumkudulu, 2016; Gaume et al., 2017b). Notably, Bruno et al. (2011) provide a general physical interpretation of the power law exponent m as a parameter accounting for the microstructure morphology. Based on FEM simulations, both Bruno et al.

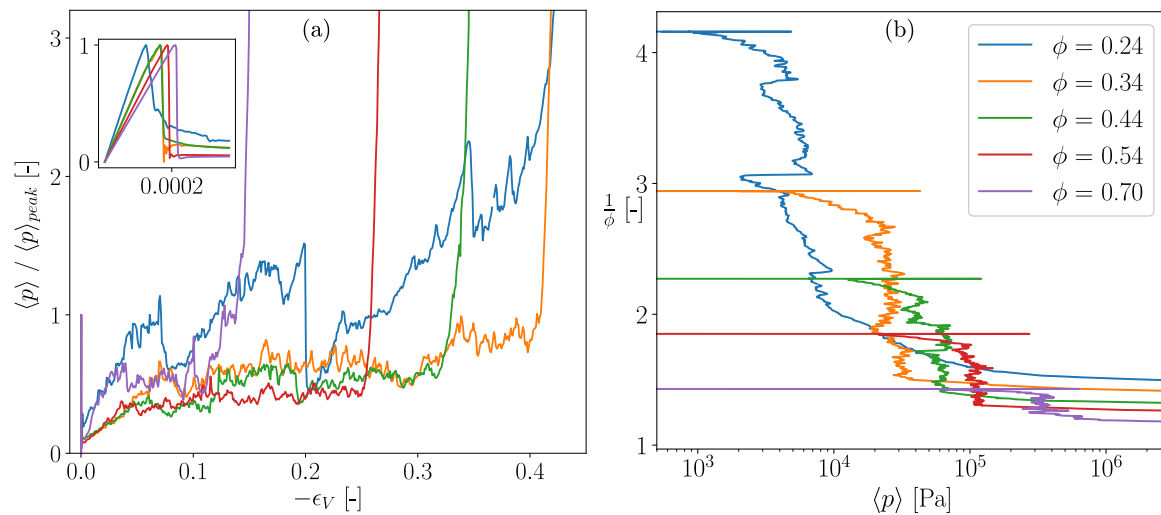


Fig. 11. Uniaxial confined compression simulations of various initial solid volume fractions ϕ . In (a), volume-averaged mean stress $\langle p \rangle$ as a function of volumetric strain ϵ_V . The inset plot shows the initial elastic and softening phase at small deformations. In (b), inverse solid volume fraction as a function of mean stress.

(2011) and Roberts and Garboczi (2000) show how m is higher when pores are star-shaped as opposed to sphere-shaped. In this view, the power law exponents reported in Eq. (14) are inherently associated with the morphology of the GRF microstructures and cannot necessarily be considered valid for any structure in general. In fact, Roberts and Garboczi (2002) and Soyarslan et al. (2018) have studied similar GRF microstructures, albeit only in the elastic regime and only for isotropic and perfectly homogeneous structures (i.e., the GRF wave vectors have a fixed magnitude). Their proposed modulus-porosity relationships do not generally give a better fit to our simulations than the simple power law proposed here for the wide range of solid volume fractions. A sensitivity analysis of the plastic parameters of the Drucker–Prager model has revealed that the power law exponents are minimally affected by the cohesion c . However, in isotropic compression, adjusting the friction γ will have a notable effect on the power law exponent. In particular, by increasing the friction angle from 30 to 50 degrees, we report an increase of 25% in this exponent. This is due to the different stress paths a porous and a dense sample will display, as can be seen by in comparing the slope of the pink curves in Fig. 7. Moreover, previous studies relying on DEM simulations of cohesive discrete spherical systems have argued that stiffness and failure onset is more sensitive to contact density than solid volume fraction alone. Contact density is the product of coordination number and solid volume fraction. These authors have proposed corresponding power laws for failure onset in the contact density, finding power law exponents between 2.5 and 3.6 (Gilabert et al., 2008; Gaume et al., 2017b; Yamaguchi et al., 2020; Ritter et al., 2020). However, in continuous structures as studied here, the coordination number cannot be straightforwardly defined as it represents the number of contacts between discrete elements.

The quadratic approximation of the failure envelopes is exceptional for the highly porous structures. However, as the solid volume fraction increases, this simple approximation overestimates the data points around vanishing mean stress (i.e., when the stress is deviatoric) which can be seen in Fig. 5b. This can be related to the determination of failure in high solid volume fraction samples in shear, in which case the second-order work displays two significant surges, e.g., as can be seen in Fig. 3b. The criterion $W_2 = 0$ can only select one of those surges as the failure point, creating a distinction between samples failing at low stress (tensile side of the envelope) or high stress (compressive side of the envelope). Nevertheless, we have chosen to keep the criterion $W_2 = 0$ due to its otherwise robust and simple character. In general, we have found the failure criterion $W_2 = 0$ to be an accurate, unambiguous and easy way of determining failure under general loading modes. This is in contrast to failure criteria such as those based on maximum shear

stress (Mede et al., 2018), initial stress peak (Gaume et al., 2017b) or a kinetic energy threshold (Ritter et al., 2020). The second order work failure criterion employed in this study was also used by Mede et al. (2020) in DEM modeling of snow under special loading condition. Moreover, our numerical experiments indicate that the quadratic failure envelope remains an excellent approximation regardless of the choice of cohesion c and friction γ in the Drucker–Prager model. In fact, the cohesion parameter c has been found to not influence the fitting constants β and M of the envelope. This is in contrast to the friction parameter γ , which clearly will bring about a decrease in β if increased. Interestingly, in Fig. 2, we evidence a general trend of increased strain at failure with increasing solid volume fraction, which is a consequence of the power law exponent being greater for the elastic modulus than for failure strength. This observation is in contrast to that of Gaume et al. (2017b) and Yamaguchi et al. (2020). Furthermore, considering only one congruent half of the parabolic envelope, the fitted envelopes are consistent with overall qualitative behavior of the Gurson/GTN models. However, these models make no distinction between dilation and compression as it assumes a perfectly plastic (von Mises) behavior for the solid phase. Performing triaxial experiments of porous carbonate, Chen et al. (2020) also suggest a quadratic fit to the failure envelope. Based on DEM simulations of porous microstructures ($\phi < 0.35$) represented as a monodisperse system of sticky hard spheres, Ritter et al. (2020) advocate an elliptic fit. Indeed, an elliptic fit for the most porous samples will also yield a reasonable match with our data. Moreover, the apparent associativity of the plastic flow is consistent with previous investigations by the same authors. Triaxial compression experiments by Wong et al. (1997) of porous sandstone support these findings, concluding that associative plastic flow is within reasonable agreement with measurements of the porosity evolution.

Propagating compaction bands as seen in our uniaxial compression simulations are consistent with experimental measurements in sandstone, e.g., by Baud et al. (2015) and in snow, e.g., by Barraclough et al. (2017). However, in the latter experiments, they observed reflection of these bands at the boundaries, which we do not reproduce in the present simulations. To account for this, the elastoplastic model can be extended to include rate-dependent mechanisms such as sintering of the material, allowing the material to strengthen over a certain characteristic time (Mulak and Gaume, 2019). As the structure with initial solid volume fraction of $\phi = 0.34$ is being compressed from the top at an imposed constant speed, the emerging compaction band propagates smoothly down the sample, and no significant stress surges are observed, see orange line in Fig. 11. On the other hand, when the initial solid volume fraction is $\phi = 0.24$, the propagation of localized

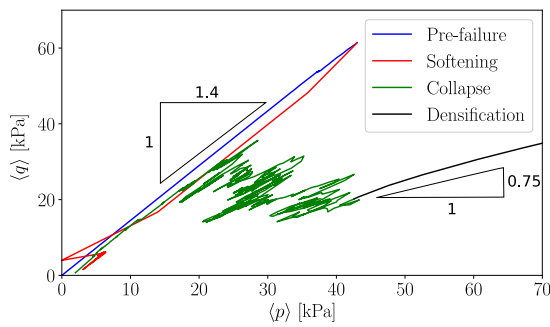


Fig. 12. Stress path followed under uniaxial confined compression simulation of a sample with initial solid volume fractions $\phi = 0.34$. The different colors mark different phases of the compression.

compaction is not completely smooth, and we observe several surges in the mean stress, plotted as the blue line in Fig. 11. During the three clearly visible stress surges at 7%, 20% and 35% compression, the localized zone of deformation will display spatial “jumps”. This is reminiscent of the experimental observations of snow by Löwe et al. (2020) whose stress–strain curves show that if snow is sufficiently consolidated, it can display significant softening surges. The serrated response observed by these authors are explained with a healing mechanism which is actually absent in the model considered here. In coupled two-dimensional FEM-DEM simulations of high-porosity sandstone ($\phi = 0.67$), Wu et al. (2020a) also report propagating compaction bands. However, their numerical studies reveal that these localized failure patterns transition to a shear band in a continuous process as the samples are compressed. On the other hand, Wu et al. (2020b) reveal in similar simulations of sandstone how the type of deformation band depends on the loading conditions. Although how failure localizes follows from structural arrangements, processes and imperfections on the microscale, it may also be considered a result of instability in the macroscopic constitutive description of plastic deformation (Rudnicki and Rice, 1975; Chambon et al., 2000). In particular, Borja and Aydin (2004) and Borja (2004) outline a mathematical framework based on bifurcation theory and demonstrate with numerical simulations the role the constitutive model and finite deformation effects play on the occurrence of shear or compaction bands in geomaterials.

Due to the plastic strain softening model, the numerical solutions will suffer from mesh dependency after yielding. Mesh dependency is a common feature in FEM modeling involving strain localization, with finer meshes typically resulting in narrower, more concentrated bands. This is also the case with MPM. To fully undertake this issue there exist several rigorous techniques of regularizing strain localization, and thus avoiding mesh dependency. Example of these methods include higher-order gradient methods (Aifantis, 1984; Vardoulakis and Aifantis, 1989), the introduction of nonlocal variables through spatially weighted averaging (Jin and Arson, 2018; Monforte et al., 2019), relying on Cosserat continuum theory (Mühlhaus and Vardoulakis, 1987), the phase-field approach (Kuhn and Müller, 2010; Ambati et al., 2015) or more recently the Lip-field approach (Moes and Chevaugeon, 2021). In various ways, they are all related to introducing characteristic length scales in the governing equations. Just as in similar recent multiscale studies (Guo and Zhao, 2014, 2016; Wu et al., 2019, 2020a,b) no such regularization scheme has been considered in this work. However, we addressed the issue of mesh dependency by taking the mesh size into the yield criterion which is a simple approach to help mitigate the influence of the mesh to the numerical solution. In particular, making the cohesion parameter c of the Drucker–Prager model dependent on mesh size can yield approximately mesh independent stress–strain response, which has been validated through numerical experiments. This is similar to the approaches employed/discussed in, e.g., Schreyer et al. (2002, 2006), Mahajan et al. (2010), Sulsky and Peterson (2011),

Zabala and Alonso (2011), Gaume et al. (2018), Garavand et al. (2020) ensuring that the same amount of energy is dissipating for different mesh resolutions. In our simulations, the error in stress–strain response resulting from mesh size has not been found to be any greater than that resulting from the morphological randomness of GRF microstructures with fixed structural parameters. As such, in this paper which has focused on the general numerical framework and broad trends rather than the accuracy of its solution to a particular problem, our approach helps mitigate mesh dependency in the sense that it produces reasonably reliable failure stresses and post-peak stress evolution. The conclusions made in this paper regarding the onset of failure, its power law and failure envelope are therefore believed not to be affected by mesh resolution. However, the localized deformation band width on the scale of the solid phase will still depend on mesh resolution.

The influence of microstructural length scales and their heterogeneity on the mechanical response has not been quantified in this work. We recall how the degree of heterogeneity is specified by the parameter b controlling the width of distribution over the GRF wave vector magnitude. This distribution can be seen as one potential continuous analogue to the grain size distribution in discrete/granular systems, see also Appendix B for more details on this. Studying the influence of grain size and its distribution requires careful considerations of finite size effects, because in this case the ratio of the system size to the microstructural length scales will vary between samples of different heterogeneity. In addition, larger representative volume elements will require finer spatial discretization, meaning that a thorough study of a sufficient number of samples can become considerably expensive from a computational point of view. Experimentally investigating granular media (sand), Rattet et al. (2020) reported that the peak stress decreases with grain size, but found no influence of the broadness of the grain size distribution. Contact dynamics simulations of granular media have reached similar conclusions regarding the influence of this distribution on shear strength (Nguyen et al., 2015; Estrada, 2016). Moreover, they observed that the shear band thickness increases with both the mean grain size and the broadness of the grain size distribution. Furthermore, Einav (2007) and Rattet et al. (2020) discuss the temporal evolution of grain size distribution during compression, suggesting that during the fragmentation process larger grains get surrounded by smaller ones, consequently providing a cushioning effect that leads to an ultimate grain size distribution. It is not clear to what extent all these observations on particulate systems translate to the continuous situation of non-particulate structures considered here, and a reliable validation of the effect of grain size distribution on shear band thickness in our numerical model is not possible as discussed in the above paragraph.

5. Conclusion

This work proposes a general and unified approach for mechanical modeling of porous brittle materials, using finite strain elastoplasticity theory, the material point method and Gaussian random field microstructures. With these ingredients, we are able to realistically simulate elasticity, failure, post-peak behavior and large deformation characteristics of geomaterials represented by arbitrary bicontinuous microstructures in a single framework. Previously, this has primarily been treated with DEM for spherical/particulate porous media only.

The numerical approach outlined here has shown that both the elastic moduli and the failure strength can be captured by a simple power law in the solid volume fraction over a wide range, from 20 to 80%. For these porous brittle materials whose solid phase can be described by a strain softening Drucker–Prager model, a basic quadratic fitting curve has been shown to reproduce the observed failure envelopes well. Moreover, we have provided evidence that an associative flow rule is appropriate, consistent with previous experimental and computational experiments. Furthermore, large deformation uniaxial compression simulations reveal that failure initially localizes in compaction

bands propagating from the top in porous samples, while as shear bands in denser samples. We have thoroughly discussed these purely numerical results in light of previous numerical and experimental observations of porous media mechanics.

The computational simulations in this study have been carefully designed to mitigate finite size effects, discretization errors and statistical structural fluctuations. We have applied our method to explore nearly homogeneous microstructural geometries resulting from single-cut Gaussian random fields. A continuation of this work may compare to other GRF based morphologies, such as the two cut, open-cell intersection or closed-cell union GRF microstructures as presented in Roberts and Garboczi (2002). Additionally, future studies can investigate the influence of heterogeneity, which is easily tunable through the GRF framework presented here. Many real structures exhibit some degree of structural anisotropy, and although not presently studied, the microstructure generation algorithm used in this work is also capable of capturing this feature. However, these future studies may entail significantly larger representative volume elements which will require considerable computational resources. Finally, another future investigation include the role of the third stress invariant on the failure and post-peak behavior.

CRediT authorship contribution statement

Lars Blatny: Investigation, Methodology, Writing – original draft, Visualization, Software, Formal analysis. **Henning Löwe:** Methodology, Supervision, Writing – review & editing. **Stephanie Wang:** Software, Writing – review & editing. **Johan Gaume:** Methodology, Conceptualization, Project administration, Supervision, Funding acquisition, Writing – review & editing.

Declaration of competing interest

The authors declare that they have no known competing financial interests or personal relationships that could have appeared to influence the work reported in this paper.

Acknowledgment

This work was supported by the Swiss National Science Foundation (grant number PCEFP2_181227).

Appendix A. Representative volume element

The relative size (i.e., the number of solid phases per unit length) of the microstructures is determined through a representative volume element convergence analysis, see Fig. A.13. The results suggests a size of at least nine mean wavelengths, in agreement with the findings of Soyarslan et al. (2018) and Chen et al. (2015) (and references therein). Thus, our computational results should not be significantly influenced by finite size effects.

Appendix B. Characteristics of the microstructures

We recall how the parameter b gives the degree of heterogeneity in the microstructures as a parameter controlling the width of the distribution over the sampled wave vector magnitudes η . We can convert this distribution into a distribution over number of wavelengths $\omega \equiv 2\pi/\eta$ per side length L of the structure, which we visualize in Fig. B.14a for various values of b . Observe that all these distributions have a mean L/ω equal to nine, as this was the size found in the representative volume element convergence analysis of Appendix A. Since, at a fixed solid volume fraction, the value of the wavelengths relates to the extent of the solid phase elements, this distribution can be thought of as one potential continuous analogue to the grain size distribution in discrete (particulate/granular) systems.

The spatial autocorrelation function (two-point correlation function) of the binary microstructure $M(\mathbf{r})$ is defined as

$$\Gamma(\mathbf{r}) = \frac{1}{V_{\text{tot}}} \int M(\mathbf{r}')M(\mathbf{r}' + \mathbf{r})d^3\mathbf{r}' \quad (\text{B.1})$$

where V_{tot} is the total solid and void volume. According to the Wiener–Khinchin theorem, it is given by the Fourier transform of the absolute squares of the Fourier coefficients of $M(\mathbf{r})$. Thus, assuming periodicity of the microstructure, we can efficiently obtain the spatial autocorrelation function through a fast Fourier transform (FFT) of the binary microstructure. Moreover, we can define $g(r)$ as the angular-averaged spatial autocorrelation function,

$$g(r) = \frac{1}{4\pi} \int_0^{2\pi} \int_0^\pi \Gamma(\mathbf{r}) \sin(\theta) d\theta d\varphi, \quad \mathbf{r} = (r, \theta, \varphi) \quad (\text{B.2})$$

Witnessing that $g(0) = \phi$ and $g(r \rightarrow \infty) = \phi^2$ we can define the normalized angular-averaged spatial autocorrelation function

$$g_{\text{norm}}(r) = \frac{g(r) - \phi^2}{\phi - \phi^2}. \quad (\text{B.3})$$

In Fig. B.14b we visualize $g_{\text{norm}}(r)$ for various levels of heterogeneity b .

We can define the specific surface area SSA as the ratio of surface area to solid volume. However, in the literature it is also common to define it as per total solid and void volume, or per solid mass. According to Berryman (1987), SSA can be found by studying the initial slope of the angular-averaged spatial autocorrelation function,

$$SSA = -\frac{4}{\phi} \lim_{r \rightarrow 0} \frac{\partial}{\partial r} g(r) \quad (\text{B.4})$$

In Fig. B.15a we visualize the measured SSA as a function of solid volume fraction and in B.15b as a function of mesh resolution. With a fixed mean wavelength and degree of heterogeneity as presented here, it is clear that SSA changes with solid volume fraction. However, with a more detailed parameter study, adjusting the structural parameters allows to independently control SSA from the solid volume fraction.

All samples studied in this work are percolating in the sense that there exists a continuous solid part of the structure that spans all sides of the sample. With a solid volume fraction approaching the percolation threshold, it becomes increasingly problematic to study the dependency with the mechanical properties as they become more dependent on arbitrary and delicate microstructural geometrical connections. As an example, we observe in Fig. 6 how the data scatter increases for decreasing solid volume fraction.

The obtained microstructure of the GRF algorithm may contain structural elements that do not belong to the percolating, side-to-side spanning, cluster. Consequently, the actual solid volume fraction ϕ may differ from the solid volume fraction ϕ_p of the underlying percolating structure. This is especially the case for highly porous samples. The quantity ϕ_p was retrieved using the burning method by Herrmann et al. (1984). As shown in Fig. B.16a, the deviation of the percolating solid volume fraction ϕ_p to that of the whole system ϕ is negligible above roughly $\phi = 0.25$. The percolation threshold for these microstructures occur at roughly $\phi = 0.15$. Using the percolating solid volume fraction ϕ_p instead of ϕ does not change the results of the paper, including the obtained power law, significantly.

We can further study the morphology of the microstructures by measuring their tortuosity, defined here as $\langle l_{\text{min}} \rangle / L$ where L is the side length and $\langle l_{\text{min}} \rangle$ is the mean minimum path length from one side of the structure to the opposite side (through either the solid or void phase). As a function of solid volume fraction, this is displayed in Fig. B.16b. Naturally, the void phase tortuosity increases and the solid phase tortuosity decreases with solid volume fraction.

Appendix C. Supplementary data

Supplementary material related to this article can be found online at <https://doi.org/10.1016/j.compgeo.2021.104284>.

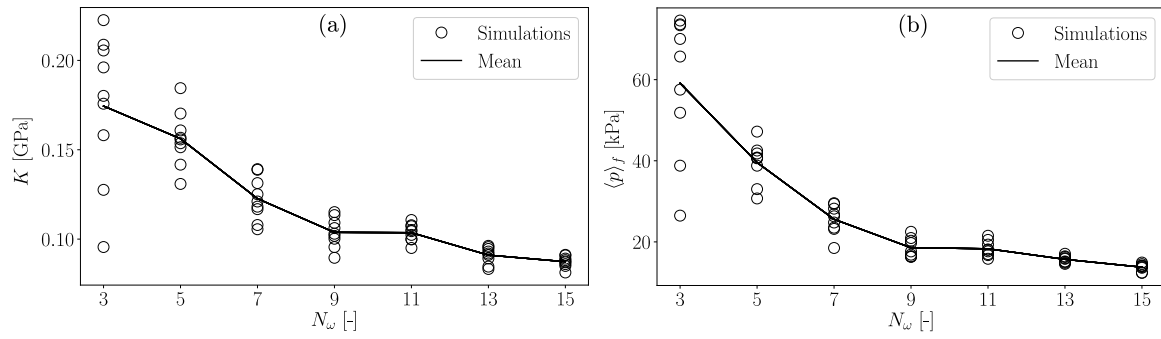


Fig. A.13. Convergence in effective bulk modulus and failure mean stress as the size of the samples increases, here measured as $N_\omega = L/\langle \omega \rangle$, i.e., the number of mean wavelengths $\langle \omega \rangle$ per cube side length L . Nine realizations are made for each statistically identical microstructure (with a solid volume fraction $\phi = 0.25$) subjected to isotropic compression loading.

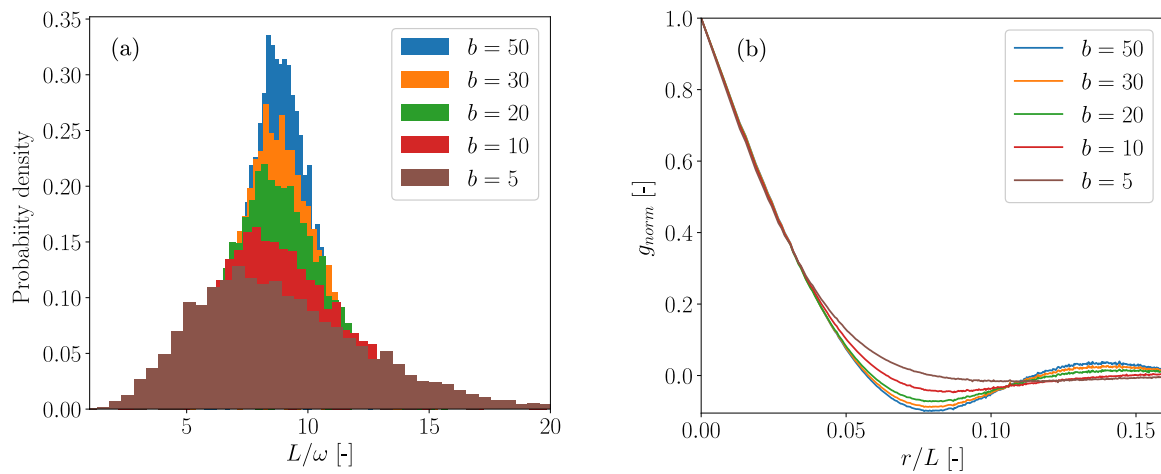


Fig. B.14. (a) Histogram over the number of wavelengths per structure side length and (b) normalized angular-averaged spatial autocorrelation function for various degrees of heterogeneity b .

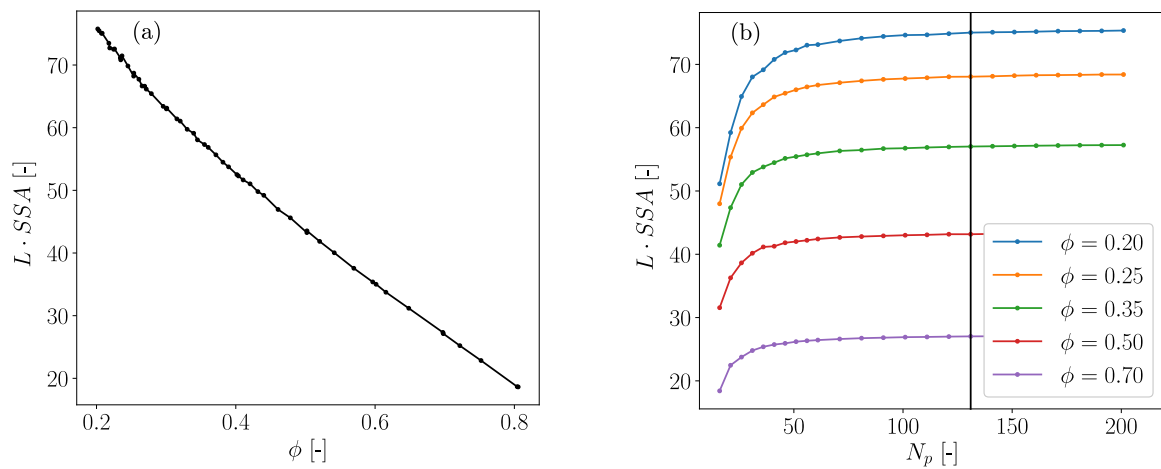


Fig. B.15. (a) Specific surface area SSA as a function of solid volume fraction ϕ for an isotropic structure with fixed mean wavelength and $b = 50$. (b) SSA as a function of mesh resolution $N_p \times N_p \times N_p$. The black vertical line indicates the resolution used throughout this paper and shows that the structure's morphology is sufficiently resolved with this choice.

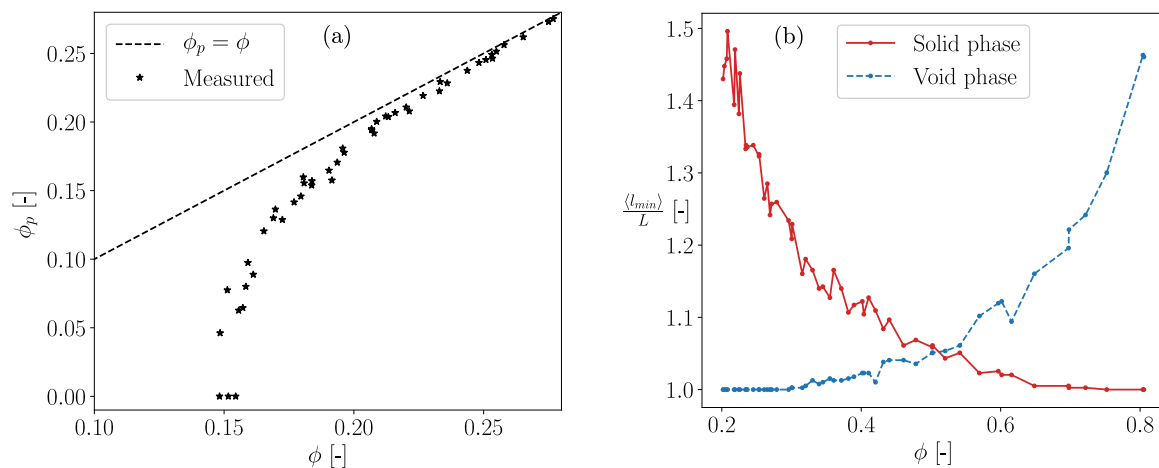


Fig. B.16. (a) Solid volume fractions ϕ_p of the percolating cluster versus the actual solid volume fractions ϕ for a set of structures with identical GRF parameters as those presented in Table 1. (b).

References

- Aexeev, V., Lavrenov, I., Smirnov, V., 2003. Estimation of the internal friction angle in sea ice cover, in: EGS - AGU - EUG Joint Assembly, Nice, abstract id. 13195.
- Aifantis, E.C., 1984. On the microstructural origin of certain inelastic models. *J. Eng. Mater. Technol.* 106, 326–330. <http://dx.doi.org/10.1115/1.3225725>.
- Ambati, M., Gerasimov, T., D. Lorenzis, L., 2015. Phase-field modeling of ductile fracture. *Comput. Mech.* 55, 1017–1040. <http://dx.doi.org/10.1007/s00466-015-1151-4>.
- Barracough, T.W., Blackford, J.R., Liebenstein, S., Sandfeld, S., Stratford, T.J., Weinländer, G., Zaiser, M., 2017. Propagating compaction bands in confined compression of snow. *Nat. Phys.* 13, 272–275. <http://dx.doi.org/10.1038/nphys3966>.
- Baud, P., Reuschlé, T., Ji, Y., Cheung, C., Wong, T.f., 2015. Mechanical compaction and strain localization in bleurswiller sandstone. *J. Geophys. Res.: Solid Earth* 120, 6501–6522. <http://dx.doi.org/10.1002/2015JB012192>.
- Berryman, J.G., 1987. Relationship between specific surface area and spatial correlation functions for anisotropic porous media. *J. Math. Phys.* 28, 244–245. <http://dx.doi.org/10.1063/1.527804>.
- Borja, R.I., 2004. Computational modeling of deformation bands in granular media. II. Numerical simulations. *Comput. Methods Appl. Mech. Eng.* 193, 2699–2718. <http://dx.doi.org/10.1016/j.cma.2003.09.018>.
- Borja, R.I., Aydin, A., 2004. Computational modeling of deformation bands in granular media. I. Geological and mathematical framework. *Comput. Methods Appl. Mech. Eng.* 193, 2667–2698. <http://dx.doi.org/10.1016/j.cma.2003.09.019>.
- Bruno, G., Efremov, A., Levandovskiy, A., Clausen, B., 2011. Connecting the macro- and microstrain responses in technical porous ceramics: modeling and experimental validations. *J. Mater. Sci.* 46, 161–173. <http://dx.doi.org/10.1007/s10853-010-4899-0>.
- Cahn, J.W., 1965. Phase separation by spinodal decomposition in isotropic systems. *J. Chem. Phys.* 42, 93–99. <http://dx.doi.org/10.1063/1.1695731>.
- Chambon, R., Crochepeyre, S., Desrues, J., 2000. Localization criteria for non-linear constitutive equations of geomaterials. *Mech. Cohes.-Frict. Mater.* 5, 61–82. [https://doi.org/10.1002/\(SICI\)1099-1484\(200001\)5:1<61::AID-CFM83>3.0.CO;2-M](https://doi.org/10.1002/(SICI)1099-1484(200001)5:1<61::AID-CFM83>3.0.CO;2-M).
- Chen, X., Roshan, H., Lv, A., Hu, M., Regenauer-Lieb, K., 2020. The dynamic evolution of compaction bands in highly porous carbonates: the role of local heterogeneity for nucleation and propagation. *Prog. Earth Planet. Sci.* 7, <http://dx.doi.org/10.1186/s40645-020-00344-0>.
- Chen, Z., Wang, X., Giuliani, F., Atkinson, A., 2015. Microstructural characteristics and elastic modulus of porous solids. *Acta Mater.* 89, 268–277. <http://dx.doi.org/10.1016/j.actamat.2015.02.014>.
- Desrues, J., Nguyen, T.K., Argilla, A., Dal Pont, S., Combe, G., Caillerie, D., 2014. Double scale numerical FEM-DEM analysis for cohesive-frictional materials. In: 10th Euroconference on Rock Physics and Rock Mechanics, Aussois, France.
- Ding, K., Xu, X., Tsang, L., 2010. Electromagnetic scattering by bicontinuous random microstructures with discrete distributions. *IEEE Trans. Geosci. Remote Sens.* 48, 3139–3151. <http://dx.doi.org/10.1109/TGRS.2010.2043953>.
- Einav, I., 2007. Breakage mechanics—Part I: Theory. *J. Mech. Phys. Solids* 55, 1274–1297. <http://dx.doi.org/10.1016/j.jmps.2006.11.003>.
- Estrada, N., 2016. Effects of grain size distribution on the packing fraction and shear strength of frictionless disk packings. *Phys. Rev. E* 94, 062903. <http://dx.doi.org/10.1103/PhysRevE.94.062903>.
- Fletcher, R.C., Pollard, D.D., 1981. Anticrack model for pressure solution surfaces. *Geology* 9, 419–424. [http://dx.doi.org/10.1130/0091-7613\(1981\)9<419:AMFPSS>2.0.CO;2](http://dx.doi.org/10.1130/0091-7613(1981)9<419:AMFPSS>2.0.CO;2).
- Fritzen, F., Forest, S., Böhlke, T., Kondo, D., Kanit, T., 2012. Computational homogenization of elasto-plastic porous metals. *Int. J. Plast.* 29, 102–119. <http://dx.doi.org/10.1016/j.ijplas.2011.08.005>.
- Garavand, A., Stefanov, Y.P., Rebetsky, Y.L., Bakeev, R.A., Myasnikov, A.V., 2020. Numerical modeling of plastic deformation and failure around a wellbore in compaction and dilation modes. *Int. J. Numer. Anal. Methods Geomech.* 44, 823–850. <http://dx.doi.org/10.1002/nag.3041>.
- Gaume, J., Gast, T., Teran, J., Herwijnen, A.van., Jiang, C., 2018. Dynamic anticrack propagation in snow. *Nature Commun.* 9, 3047. <http://dx.doi.org/10.1038/s41467-018-05181-w>.
- Gaume, J., van Herwijnen, A.van., Chambon, G., Wever, N., Schweizer, J., 2017a. Snow fracture in relation to slab avalanche release: critical state for the onset of crack propagation. *Cryosphere* 11, 217–228. <http://dx.doi.org/10.5194/tc-2016-64>.
- Gaume, J., Löwe, H., Tan, S., Tsang, L., 2017b. Scaling laws for the mechanics of loose and cohesive granular materials based on Baxter's sticky hard spheres. *Phys. Rev. E* 96, 032914. <http://dx.doi.org/10.1103/PhysRevE.96.032914>.
- Gibson, I.J., Ashby, M.F., 1982. The mechanics of three-dimensional cellular materials. *Proc. R. Soc. Lond. Ser. A Math. Phys. Eng. Sci.* 382, 43–59. <http://dx.doi.org/10.1098/rspa.1982.0088>.
- Gilbert, F.A., Roux, J.N., Castellanos, A., 2008. Computer simulation of model cohesive powders: Plastic consolidation, structural changes, and elasticity under isotropic loads. *Phys. Rev. E* 78, 031305. <http://dx.doi.org/10.1103/PhysRevE.78.031305>.
- Green, H.W., Young, T.E., Walker, D., Scholz, C.H., 1990. Anticrack-associated faulting at very high pressure in natural olivine. *Nature* 348, 720–722. <http://dx.doi.org/10.1038/348720a0>.
- Guillard, F., Golshan, P., Shen, L., Valdes, J.R., Einav, I., 2015. Dynamic patterns of compaction in brittle porous media. *Nat. Phys.* 11, <http://dx.doi.org/10.1038/nphys3424>.
- Guo, N., Zhao, J., 2014. A coupled FEM/DEM approach for hierarchical multiscale modelling of granular media. *Internat. J. Numer. Methods Engrg.* 99, 789–818. <http://dx.doi.org/10.1002/nme.4702>.
- Guo, N., Zhao, J., 2016. 3D multiscale modeling of strain localization in granular media. *Comput. Geotech.* 80, 360–372. <http://dx.doi.org/10.1016/j.compgeo.2016.01.020>.
- Gurson, A.L., 1977. Continuum theory of ductile rupture by void nucleation and growth: Part I—Yield criteria and flow rules for porous ductile media. *J. Eng. Mater. Technol.* 99, 2–15. <http://dx.doi.org/10.2172/7351470>.
- Hagenmuller, P., Chambon, G., Naaim, M., 2015. Microstructure-based modeling of snow mechanics: a discrete element approach. *Cryosphere* 9, 1969–1982. <http://dx.doi.org/10.5194/tc-9-1969-2015>.
- Hashin, Z., Shtrikman, S., 1963. A variational approach to the theory of the elastic behaviour of multiphase materials. *J. Mech. Phys. Solids* 11, 127–140. [http://dx.doi.org/10.1016/0022-5096\(63\)90060-7](http://dx.doi.org/10.1016/0022-5096(63)90060-7).
- Heierli, J., Gumbsch, P., Zaiser, M., 2008. Anticrack nucleation as triggering mechanism for snow slab avalanches. *Science* 321, 240–243. <http://dx.doi.org/10.1126/science.1153948>.
- Herrmann, H.J., Hong, D.C., Stanley, H.E., 1984. Backbone and elastic backbone of percolation clusters obtained by the new method of burning. *J. Phys. A: Math. Gen.* 17, L261–L266. <http://dx.doi.org/10.1088/0305-4470/17/5/008>.
- Hill, R., 1958. A general theory of uniqueness and stability in elastic-plastic solids. *J. Mech. Phys. Solids* 6, 236–249. [http://dx.doi.org/10.1016/0022-5096\(58\)90029-2](http://dx.doi.org/10.1016/0022-5096(58)90029-2).
- Jin, W., Arson, C., 2018. Nonlocal enrichment of a micromechanical damage model with tensile softening: Advantages and limitations. *Comput. Geotech.* 94, 196–206. <http://dx.doi.org/10.1016/j.compgeo.2017.09.011>.
- Klár, G., Gast, T., Pradhana, A., Fu, C., Schroeder, C., Jiang, C., Teran, J., 2016. Drucker-Prager elastoplasticity for sand animation. *ACM Trans. Graph.* 35, 1–12. <http://dx.doi.org/10.1145/2897824.2925906>.

- Kuhn, C., Müller, R., 2010. A continuum phase field model for fracture. *Eng. Fract. Mech.* 77, 3625–3634. <http://dx.doi.org/10.1016/j.engfracmech.2010.08.009>.
- Löwe, H., Zaiser, M., Mösinger, S., Schlee, S., 2020. Snow mechanics near the ductile–brittle transition: compressive stick–slip and snow microquakes. *Geophys. Res. Lett.* 47, 1–9. <http://dx.doi.org/10.1029/2019GL085491>.
- Mahajan, P., Kalakuntla, R., Chandel, C., 2010. Numerical simulation of failure in a layered thin snowpack under skier load. *Ann. Glaciol.* 51, 169–175. <http://dx.doi.org/10.3189/172756410791386436>.
- Mast, C.M., 2013. Modeling landslide-induced flow interactions with structures using the material point method. (Ph.D. thesis). University of Washington, Seattle.
- Mede, T., Chambon, G., Hagenmuller, P., Nicot, F., 2018. Snow failure modes under mixed loading. *Geophys. Res. Lett.* 45 (13), 351–358. <http://dx.doi.org/10.1029/2018GL080637>.
- Mede, T., Chambon, G., Nicot, F., Hagenmuller, P., 2020. Micromechanical investigation of snow failure under mixed-mode loading. *Int. J. Solids Struct.* 199, 95–108. <http://dx.doi.org/10.1016/j.ijsolstr.2020.04.020>.
- Mewis, J., Wagner, N.J., 2011. Colloidal Suspension Rheology. In: Cambridge Series in Chemical Engineering, Cambridge University Press, <http://dx.doi.org/10.1017/CBO9780511977978>.
- Moes, N., Chevaugeon, N., 2021. Lipschitz Regularization for softening material models: the Lip-field approach. [arXiv:2103.16345](https://arxiv.org/abs/2103.16345).
- Monforte, L., Ciantia, M.O., Carbonell, J.M., Arroyo, M., Gens, A., 2019. A stable mesh-independent approach for numerical modelling of structured soils at large strains. *Comput. Geotech.* 116, 103215. <http://dx.doi.org/10.1016/j.compgeo.2019.103215>.
- Mühlhaus, H.B., Vardoulakis, I., 1987. The thickness of shear bands in granular materials. *Géotechnique* 37, 271–283. <http://dx.doi.org/10.1680/geot.1987.37.3.271>.
- Mulak, D., Gaume, J., 2019. Numerical investigation of the mixed-mode failure of snow. *Comput. Part. Mech.* 6, 439–447. <http://dx.doi.org/10.1007/s40571-019-00224-5>.
- Nguyen, D.H., Azéma, E., Sornay, P., Radjai, F., 2015. Effects of shape and size polydispersity on strength properties of granular materials. *Phys. Rev. E* 91, 032203. <http://dx.doi.org/10.1103/PhysRevE.91.032203>.
- Nicot, F., Darve, F., 2015. Describing failure in geomaterials using second-order work approach. *Water Sci. Eng.* 8, 89–95. <http://dx.doi.org/10.1016/j.wse.2015.05.001>.
- Nicot, F., Lerbet, J., Darve, F., 2017. Second-order work criterion: from material point to boundary value problems. *Acta Mech.* 228, 2483–2498. <http://dx.doi.org/10.1007/s00707-017-1844-1>.
- Nicot, F., Sibille, L., Darve, F., 2009. Bifurcation in granular materials: An attempt for a unified framework. *Int. J. Solids Struct.* 46, 3938–3947. <http://dx.doi.org/10.1016/j.ijsolstr.2009.07.008>.
- Petit, C., Meille, S., Maire, E., 2013. Cellular solids studied by x-ray tomography and finite element modeling – a review. *J. Mater. Res.* 28, 2191–2201. <http://dx.doi.org/10.1557/jmr.2013.97>.
- Petrovic, J.J., 2003. Review mechanical properties of ice and snow. *J. Mater. Sci.* 38, 1–6. <http://dx.doi.org/10.1023/A:1021134128038>.
- Rattez, H., Shi, Y., Sac-Morane, A., Klaeyle, T., Mielniczuk, B., Veveakis, M., 2020. Effect of grain size distribution on the shear band thickness evolution in sand. *Géotechnique* 1–14. <http://dx.doi.org/10.1680/jgeot.20.P.120>.
- Ritter, J., Gaume, J., Löwe, H., 2020. Microstructural controls of anticrack nucleation in highly porous brittle solids. *Sci. Rep.* 10, <http://dx.doi.org/10.1038/s41598-020-67926-2>.
- Roberts, A.P., Garboczi, E.J., 2000. Elastic properties of model porous ceramics. *J. Am. Ceram. Soc.* 83, 3041–3048. <http://dx.doi.org/10.1111/j.1151-2916.2000.tb01680.x>.
- Roberts, A.P., Garboczi, E.J., 2002. Computation of the linear elastic properties of random porous materials with a wide variety of microstructure. *Proc. R. Soc. Lond. Ser. A Math. Phys. Eng. Sci.* 458, 1033–1054. <http://dx.doi.org/10.1098/rspa.2001.0900>.
- Roy, S., Tirumkudulu, M.S., 2016. Yielding in a strongly aggregated colloidal gel. Part I: 2D simulations. *J. Rheol.* 60, 559–574. <http://dx.doi.org/10.1122/1.4948324>.
- Rudnicki, J., Rice, J., 1975. Conditions for the localization of deformation in pressure-sensitive dilatant materials. *J. Mech. Phys. Solids* 23, 371–394. [http://dx.doi.org/10.1016/0022-5096\(75\)90001-0](http://dx.doi.org/10.1016/0022-5096(75)90001-0).
- Schreyer, H.L., Sulsky, D.L., Munday, L.B., Coon, M.D., Kwok, R., 2006. Elastic–decohesive constitutive model for sea ice. *J. Geophys. Res. Oceans* 111, <http://dx.doi.org/10.1029/2005JC003334>.
- Schreyer, H., Sulsky, D., Zhou, S.J., 2002. Modeling delamination as a strong discontinuity with the material point method. *Comput. Methods Appl. Mech. Engrg.* 191, 2483–2507. [http://dx.doi.org/10.1016/S0045-7825\(01\)00409-1](http://dx.doi.org/10.1016/S0045-7825(01)00409-1).
- Silva, M.J., Gibson, L.J., 1997. The effects of non-periodic microstructure and defects on the compressive strength of two-dimensional cellular solids. *Int. J. Mech. Sci.* 39, 549–563. [http://dx.doi.org/10.1016/S0020-7403\(96\)00065-3](http://dx.doi.org/10.1016/S0020-7403(96)00065-3).
- Soyarslan, C., Bargmann, S., Pradas, M., Weissmüller, J., 2018. 3D stochastic bicontinuous microstructures: Generation, topology and elasticity. *Acta Mater.* 149, 326–340. <http://dx.doi.org/10.1016/j.actamat.2018.01.005>.
- Sternlof, K.R., Rudnicki, J.W., Pollard, D.D., 2005. Anticrack inclusion model for compaction bands in sandstone. *J. Geophys. Res.: Solid Earth* 110, <http://dx.doi.org/10.1029/2005JB003764>.
- Sulsky, D., Chen, Z., Schreyer, H.L., 1994. A particle method for history-dependent materials. *Comput. Methods Appl. Mech. Engrg.* 118, 179–196. [http://dx.doi.org/10.1016/0045-7825\(94\)90112-0](http://dx.doi.org/10.1016/0045-7825(94)90112-0).
- Sulsky, D., Peterson, K., 2011. Toward a new elastic–decohesive model of arctic sea ice. *Physica D* 240, 1674–1683. <http://dx.doi.org/10.1016/j.physd.2011.07.005>.
- Tan, S., Xiong, C., Xu, X., Tsang, L., 2016. Uniaxial effective permittivity of anisotropic bicontinuous random media using NMM3D. *IEEE Geosci. Remote Sens. Lett.* 13, 1168–1172. <http://dx.doi.org/10.1109/LGRS.2016.2574759>.
- Tvergaard, V., 1981. Influence of voids on shear band instabilities under plane strain conditions. *Int. J. Fract.* 17, 389–407. <http://dx.doi.org/10.1007/BF00036191>.
- Tvergaard, V., Needleman, A., 1984. Analysis of the cup-cone fracture in a round tensile bar. *Acta Metall.* 32, 157–169. [http://dx.doi.org/10.1016/0001-6160\(84\)90213-X](http://dx.doi.org/10.1016/0001-6160(84)90213-X).
- Vardoulakis, I., Aifantis, E.C., 1989. Gradient dependent dilatancy and its implications in shear banding and liquefaction. *Ing. Arch.* 59, 197–208. <http://dx.doi.org/10.1007/BF00532250>.
- Wong, T.f., David, C., Zhu, W., 1997. The transition from brittle faulting to cataclastic flow in porous sandstones: Mechanical deformation. *J. Geophys. Res.: Solid Earth* 102, 3009–3025. <http://dx.doi.org/10.1029/96JB03281>.
- Wu, H., Zhao, J., Guo, N., 2019. Multiscale modeling of compaction bands in saturated high-porosity sandstones. *Eng. Geol.* 261, 105282. <http://dx.doi.org/10.1016/j.enggeo.2019.105282>.
- Wu, H., Zhao, J., Liang, W., 2020a. Pattern transitions of localized deformation in high-porosity sandstones: Insights from multiscale analysis. *Comput. Geotech.* 126, 103733. <http://dx.doi.org/10.1016/j.compgeo.2020.103733>.
- Wu, H., Zhao, J., Liang, W., 2020b. The signature of deformation bands in porous sandstones. *Rock Mech. Rock Eng.* 53, 3133–3147. <http://dx.doi.org/10.1007/s00603-020-02100-8>.
- Yamaguchi, Y., Biswas, S., Hatano, T., Goehring, L., 2020. Failure processes of cemented granular materials. [arXiv e-prints, arXiv:2007.08367](https://arxiv.org/abs/2007.08367).
- Zabala, F., Alonso, E., 2011. Progressive failure of Aznalcóllar dam using the material point method. *Géotechnique* 61, 795–808. <http://dx.doi.org/10.1680/geot.9.P.134>.
- Zhang, W., Wang, D., Randolph, M.F., Puzrin, A.M., 2015. Catastrophic failure in planar landslides with a fully softened weak zone. *Géotechnique* 65, 755–769. <http://dx.doi.org/10.1680/geot14.P.218>.
- Zhao, S., Zhao, J., Lai, Y., 2020. Multiscale modeling of thermo-mechanical responses of granular materials: A hierarchical continuum–discrete coupling approach. *Comput. Methods Appl. Mech. Engrg.* 367, 113100. <http://dx.doi.org/10.1016/j.cma.2020.113100>.